coatings

MDPI

Article

Influence of Anodic Oxidation on the Organizational Structure and Corrosion Resistance of Oxide Film on AZ31B Magnesium Alloy

Yuxin Kang [1], Shufang Yan [1,2], Zhanlin Li [1], Zhigang Wang [3], Ao Yang [1], Wen Ma [1], Weidong Chen [1,2,*] and Yinhui Qu [4,*]

[1] School of Materials Science and Engineering, Inner Mongolia University of Technology, Hohhot 010051, China; zanessa2024@163.com (Y.K.); lizhanlin2021@163.com (Z.L.)
[2] Inner Mongolia Autonomous Region Key Laboratory of Film and Coatings, Hohhot 010051, China
[3] School of Materials and Metallurgy, Inner Mongolia University of Science & Technology, Baotou 014010, China; wangzhigang@imust.edu.cn
[4] Shenyang Research Institute of Foundry Co., Ltd. (SRIF), Shenyang 110022, China
* Correspondence: weidongch@163.com (W.C.); qyhsky@163.com (Y.Q.)

Abstract: Magnesium alloys, notably AZ31B, hold promise for lightweight structural applications in the aerospace, automotive, and biomedical sectors due to their excellent strength-to-weight ratios. The broad adoption of these alloys, however, is hindered by their inherent susceptibility to corrosion, reducing durability and functional integrity in corrosive environments. This study explores anodic oxidation as a viable surface treatment to improve the corrosion resistance of the AZ31B magnesium alloy. Focusing on the impact of oxidation voltage on the oxide film's structural and electrochemical properties, we aim to optimize these characteristics to enhance the alloy's utility and lifespan significantly. Through detailed analysis of surface and cross-sectional morphologies, film thickness, phase composition, and corrosion resistance, we identify an optimal oxidation voltage of 17.5 V that notably improves the oxide film's density and corrosion resistance. Through this research, we contribute to the ongoing efforts to overcome the corrosion vulnerability of magnesium alloys, thereby unlocking their full potential in contributing to more sustainable and efficient technological advancements.

Keywords: AZ31B magnesium alloy; anodic oxidation; oxidation voltage; electrochemistry; corrosion resistance

Citation: Kang, Y.; Yan, S.; Li, Z.; Wang, Z.; Yang, A.; Ma, W.; Chen, W.; Qu, Y. Influence of Anodic Oxidation on the Organizational Structure and Corrosion Resistance of Oxide Film on AZ31B Magnesium Alloy. *Coatings* **2024**, *14*, 271. https://doi.org/10.3390/coatings14030271

Academic Editor: Alina Vladescu

Received: 31 January 2024
Revised: 17 February 2024
Accepted: 20 February 2024
Published: 23 February 2024

1. Introduction

Magnesium alloys are known for their low density, good electrical and thermal conductivity, high specific stiffness and strength, and excellent impact resistance [1,2]. They are among the lightest structural materials in current engineering applications. These alloys find widespread use in various fields, including electronics and telecommunications, automotive transportation, and energy materials [3,4]. Among these, the AZ31B magnesium alloy is particularly notable for its optimal balance of mechanical properties and workability. However, the widespread adoption of AZ31B and similar magnesium alloys is significantly limited by their inherent susceptibility to corrosion [5], particularly in aggressive environments. The naturally formed oxide film on magnesium alloys is porous and loose [6], offering inadequate protection to the substrate and limiting its long-term functionality in corrosive environments [7]. Therefore, improving the corrosion resistance of magnesium alloys has become a key issue in its application.

There are mainly two approaches to enhance the corrosion resistance of magnesium alloys: one is through alloying to optimize the microstructure of the magnesium alloy substrate, and the other is through surface treatment techniques to obtain a protective film

with excellent corrosion resistance on the magnesium alloy surface [8]. Surface treatment techniques are advantageous for their simplicity, low cost, and effective protection, making them the most effective and commonly used means to improve the corrosion resistance of magnesium alloys.

Surface treatment techniques have been at the forefront of efforts to mitigate corrosion in magnesium alloys. Chemical conversion coatings, including chromium and phosphate-based methods, have been extensively used to confer protective properties on magnesium surfaces. Nevertheless, the environmental hazards associated with some of these chemicals have prompted the exploration of safer alternatives [9,10]. Organic coatings offer a less toxic route but may lack the durability required for effective long-term protection [11]. Plasma electrolytic oxidation (PEO) has been lauded for its superior corrosion resistance, attributed to the formation of hard ceramic-like oxide layers; however, its adoption is hindered by high operational costs and energy consumption [12,13]. Alloying has also been investigated as a means to inherently improve corrosion resistance, with aluminum, zinc, and rare earth elements being common additives. These strategies have yielded mixed results, often complicating alloy properties and processing [14,15].

Against this backdrop, anodic oxidation emerges as a promising technique for enhancing the corrosion resistance of magnesium alloys. Distinguished by its ability to form a protective oxide layer directly from the magnesium alloy substrate, anodic oxidation offers a simpler, more environmentally friendly approach to surface treatment [16,17]. This method ensures uniform coverage and strong adhesion of the oxide layer, addressing some of the key limitations of traditional coatings.

Our study focuses on the AZ31B magnesium alloy, selected for its widespread industrial use and significant potential for performance enhancement through optimized surface treatment. The choice of anodic oxidation, conducted under constant voltage conditions, is predicated on its advantages in terms of process control, environmental sustainability, and effectiveness in improving corrosion resistance. Unlike previous research, which often lacked comprehensive optimization of the oxidation parameters, our work systematically investigates the impact of oxidation voltage on the oxide film's morphology, phase composition, and electrochemical properties. This detailed examination aims to identify optimal conditions that yield the best combination of protective qualities, thereby extending the alloy's usability in its intended applications.

In summary, this study contributes to the field by presenting a novel approach to the anodic oxidation of AZ31B magnesium alloy, optimizing the process to achieve superior corrosion resistance. Through a combination of morphological, compositional, and electrochemical analyses, we uncover the conditions under which the anodic oxide film offers the most effective protection against corrosion. These findings not only advance our understanding of the corrosion protection mechanisms for magnesium alloys but also provide a basis for the development of more durable, lightweight materials for advanced engineering applications.

2. Experiment

2.1. Preparation Method

The AZ31B magnesium alloy was selected as the experimental material. The alloy was cut into rectangular samples of 30 mm × 20 mm × 4 mm using a wire-cutting method. A hole of diameter φ5 mm was drilled in the center of the top of each sample for suspension during the anodic oxidation experiment. The samples were polished, ultrasonically cleaned in anhydrous ethanol, and then rinsed with deionized water before being dried for use.

For the anodic oxidation treatment, pre-prepared magnesium alloy specimens were used as the anode, and graphite rod electrodes served as the cathode. This process was conducted under constant temperature water bath conditions using a direct current anodic oxidation device. Ion transmission uniformity during the anodic oxidation process was maintained using a magnetic stirrer. The basic electrolyte consisted of 10 g/L $MgCl_2$, 15 g/L $Na_2SiO_3 \cdot 9H_2O$, 5 mL/L ethylene glycol, and 0.5 g/L ethylenediaminetetraacetic

acid (EDTA), prepared using deionized water. An adjustable constant voltage direct current was applied at 10 V, 12.5 V, 15 V, 17.5 V, and 20 V to the samples for anodic oxidation treatment for 3 min. After oxidation, the samples were rinsed with deionized water and dried with hot air.

2.2. Detection and Analysis

The surface and cross-sectional morphologies of the anodically oxidized films on AZ31B magnesium alloy were observed using a FEI QUANTA 650 FEG Field Emission Scanning Electron Microscope. The film thickness of the anodically oxidized samples was measured at five different points on both sides of each sample using an AT240 film thickness gauge (MINITEST 745). The crystal phase structure of the anodic oxidation film layer was detected using a Rigaku D/max-2500PC X-ray diffractometer (Tokyo, Japan), analyzing the phase composition of the anodic oxide film on the surface of AZ31B magnesium alloy.

Electrochemical Potentiodynamic Polarization (PDP) and Electrochemical Impedance Spectroscopy (EIS) tests on the anodically oxidized film layer of AZ31B magnesium alloy were conducted using a Zahner Electrochemical Workstation. A three-electrode electrolytic cell configuration was employed, with a saturated calomel electrode (SCE) as the reference electrode, a platinum (Pt) electrode as the auxiliary electrode, and the AZ31B magnesium alloy sample as the working electrode. A 3.5% NaCl solution, prepared using deionized water to simulate a seawater environment, served as the corrosive solution [18]. The samples were stabilized in the solution for 10 min before testing to achieve a stable system state, and the open circuit potential (OCP) was tested for 1 h. Subsequently, EIS tests were performed with a frequency sweep range from 10^{-2} to 10^{5} Hz [19]. Finally, PDP tests were conducted, with the polarization curve potential sweep range from −1.5 to 1.5 V at a scan rate of 5 mV/s. The corrosion potential (E_{corr}) and corrosion current density (J_{corr}) of the AZ31B magnesium alloy samples were determined through Tafel extrapolation fitting.

3. Results

3.1. Morphology of the Anodic Oxide Film on AZ31B Magnesium Alloy

Figure 1 presents the surface morphology of the anodic oxide film on AZ31B magnesium alloy prepared under different voltages. As observed from Figure 1, the anodic oxide film on AZ31B magnesium alloy is characterized by unevenly distributed micropores formed due to discharge and gas release, along with a significant presence of microcracks [20–22]. As the voltage increases, there is a noticeable improvement in the discharge phenomenon. The number of micropores on the film surface slightly decreases, their average diameter reduces, and the overall surface becomes smoother, denser, and more uniformly distributed. However, there are still some larger interconnected micropores.

At an anodic oxidation voltage of 10 V, the film surface exhibits a "tumor-like" protruding structure, with microcracks on the surface of the protrusions. These cracks tend to initiate and expand with the intensification of the oxidation reaction [23]. At 12.5 V, the microcracks begin to grow, and a larger discharge phenomenon occurs as the oxidation voltage increases. The formation of gas overflow channels during the oxidation process and the retention of gas within the film layer lead to localized pore formation in the film [24]. When the voltage reaches 15 V, the film surface shows a flat, lamellar structure with loosely connected layers and notable large cracks and collapses [25]. At 17.5 V, there are large through-holes on the surface, along with some small micropores and tiny microcracks [26]. This is primarily due to the discharge and gas release during the anodic oxidation of the magnesium alloy surface [27]. However, the film layer is relatively smoother and denser overall. At 20 V, the surface exhibits a large number of molten material protrusions and coarse cracks. As these cracks expand, multiple pores form, reducing the levelness of the film, which gradually becomes incomplete, and its overall roughness increases. The emergence of large cracks is mainly related to the difference in the thermal expansion coefficient between the film layer and the substrate, as well as the expansion of microcracks [26].

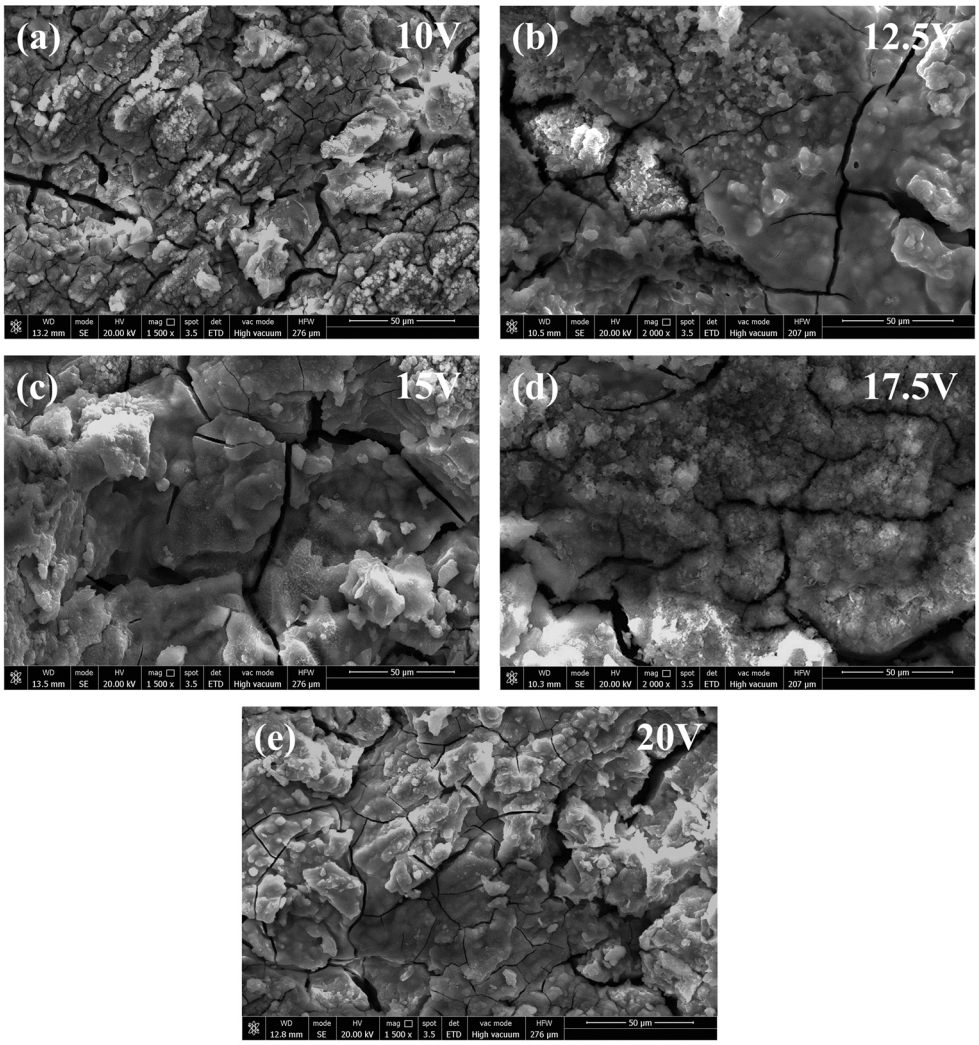

Figure 1. Surface morphology of AZ31B magnesium alloy anodic oxide film prepared at different voltages: (**a**) 10 V; (**b**) 12.5 V; (**c**) 15 V; (**d**) 17.5 V and (**e**) 20 V.

Figure 2 illustrates the cross-sectional morphology of the anodic oxide film on AZ31B magnesium alloy prepared under various voltages. As shown in Figure 2, the oxide film layer of AZ31B magnesium alloy exhibits an "interlocking" connection with the substrate, a characteristic due to the in situ growth of the anodic oxide film, resulting in an indistinct boundary between the film and the substrate [28,29]. The film layer internally harbors pores and cracks of varying sizes and depths; yet, overall, it maintains a relatively good adhesion with the substrate.

At an anodic oxidation voltage of 10 V, the film thickness is minimal, featuring crack defects and micropores, with the boundary between the loose and dense layers not being distinctly visible. At 12.5 V, the film thickness slightly increases, but deeper cracks appear, and parts of the film layer exhibit delamination. When the voltage is increased to 15 V, the continuous oxidation process leads to an increase in film thickness to a certain extent, making it difficult for the intensified anodic oxidation voltage to penetrate the film layer. Discharge consistently occurs in the film's weakest areas, constantly shifting [30]. Consequently, collapsing and cracking become more pronounced, large pores emerge on the film surface, and numerous cracks develop at the juncture of the outer loose layer and the inner dense layer, leading to a reduction in the film's adhesion strength. At 17.5 V, due to the increased anodic oxidation voltage, the driving force for film growth is enhanced, and the discharge energy gradually rises, accelerating the reaction towards the substrate interior. This results in a noticeable increase in the film thickness. Although there are no distinct

loose and dense layers, the internal film layer's overall adherence to the substrate is more uniform and compact. However, at 20 V, current efficiency decreases. Excessive voltage during electrolysis produces an excess of oxygen gas, impacting the film layer significantly and causing brittleness or delamination [31,32]. Moreover, the growth rate and dissolution rate of the film layer reach a dynamic equilibrium, preventing further thickening of the film. The outer loose film layer exhibits numerous pores and cracks, with the dual-layer film structure not being tightly bound and displaying delamination. The inner dense layer contains a wide distribution of pores, a consequence of the increased voltage leading to a high reaction rate. This prevents the subsequently formed molten material from quickly filling the pores formed in earlier stages, ultimately resulting in a large number of closed micropores within the film layer.

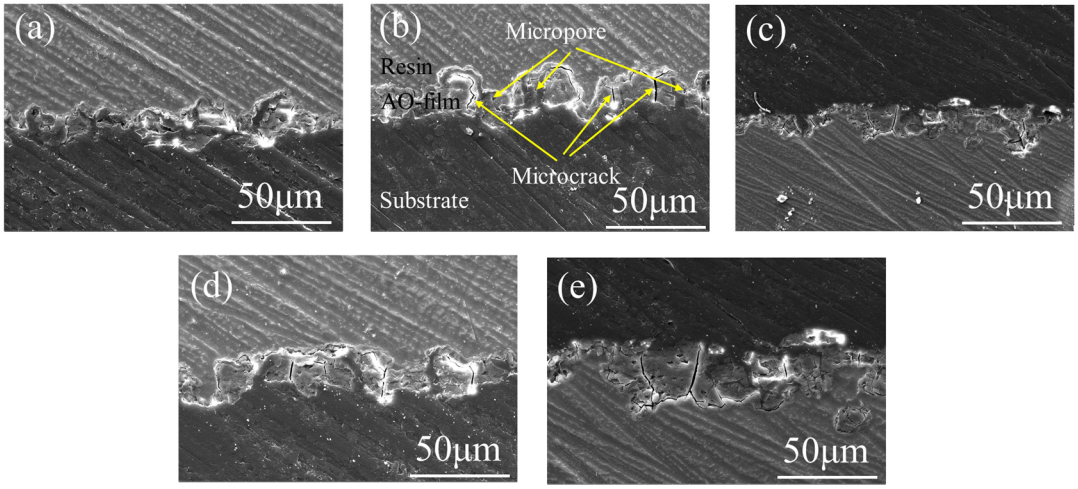

Figure 2. Cross-section morphology of AZ31B magnesium alloy anodic oxide film prepared at different voltages: (**a**) 10 V; (**b**) 12.5 V; (**c**) 15 V; (**d**) 17.5 V and (**e**) 20 V.

3.2. Thickness of the Anodic Oxide Film on AZ31B Magnesium Alloy

Figure 3 displays the thickness of the anodic oxide film on AZ31B magnesium alloy prepared under different voltages. As indicated in Figure 3, the thicknesses of the anodic oxide films prepared at varying oxidation voltages were 10.6 μm, 10.9 μm, 14.7 μm, 19.5 μm, and 17.6 μm, respectively. The trend shows an initial increase followed by a decrease in film thickness with rising voltage. With the increase in anodic oxidation voltage, the reactions associated with film re-penetration and molten growth become more intense, enhancing the film formation driving force and accelerating the growth rate of the film. This process alters the originally dense film structure, creating new pores and microcracks, allowing the anodic oxidation electrolyte to penetrate into the interior of the film. Near the metal surface, the oxide film continuously dissolves and regenerates, a cycle that repeats with changing oxidation voltage, ultimately resulting in a thicker anodic oxide film. As the anodic oxidation voltage increases, the energy input on the film surface grows, enhancing the oxidation efficiency of the AZ31B magnesium alloy surface and leading to faster film growth, thus gradually thickening the film [33–36]. However, once the anodic oxidation voltage exceeds a certain threshold, the energy of each pulse discharge becomes excessive, impeding the stable growth of the film. Consequently, the film ceases to thicken beyond a certain point. Excessive anodic oxidation voltage reduces current efficiency and generates a large amount of oxygen during electrolysis, exerting significant pressure on the film, leading to brittleness or delamination of the oxide film layer [37]. Therefore, when the anodic oxidation voltage reaches its maximum of 20 V, the film thickness begins to decrease. As the anodic oxidation voltage increases from 17.5 V to 20 V, the current significantly drops, rapidly equilibrating the film layer's temperature with that of the electrolyte. Due to uneven volume shrinkage and larger micropore diameters, the film becomes relatively loose, ultimately resulting in film delamination and a decrease in film thickness from

19.5 μm to 17.6 μm. At an anodic oxidation voltage of 17.5 V, the film achieves its maximum thickness of 19.5 μm. Combined with its microstructural morphology, the film layer under this anodic oxidation voltage is relatively smoother, denser, and exhibits a more uniform and compact integration with the substrate.

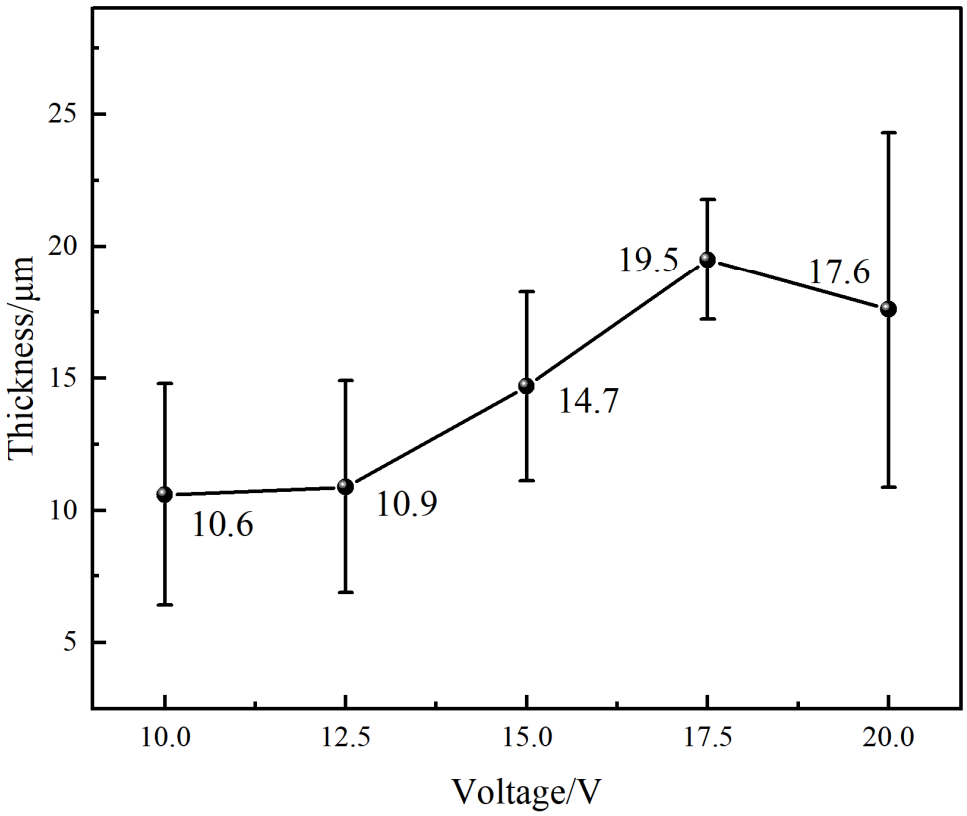

Figure 3. Thickness of AZ31B magnesium alloy anodic oxide film prepared at different voltages.

3.3. Phase Composition of the Anodic Oxide Film on AZ31B Magnesium Alloy

Figure 4 presents the X-ray Diffraction (XRD) spectra of the anodic oxide film on AZ31B magnesium alloy. As indicated in Figure 4, the phase composition of the anodic oxide film layer on AZ31B magnesium alloy primarily includes MgO and Mg_2SiO_4 phases, along with the diffraction peaks of the Mg matrix. In the discharge environment, Na_2SiO_3 in the anodic oxidation electrolyte readily hydrolyzes, forming SiO_3^{2-}, which combines with OH^- in the solution to form $Si(OH)_4$. $Si(OH)_4$ further dehydrates to form SiO_2 [38]. As anodic oxidation progresses, continuous surface discharge releases substantial energy, causing Mg in the AZ31B magnesium alloy substrate to dissolve into Mg^{2+} ions in a plasma state under the influence of an external power source. The high temperature microzone created by the discharge promotes thermal diffusion of Mg^{2+} along the discharge channels into the film layer. Here, they react with OH^- anions, which migrate to the film–electrolyte interface under the electric field and deposit within the discharge channels as MgO [39,40]. When these growth elements encounter each other, under thermodynamic stimulation, SiO_2 and MgO melt at high temperatures, undergo a phase change, and ultimately form a mixed oxide of Mg_2SiO_4 and MgO. The reactions can be summarized as follows [41–43]:

$$Mg \rightarrow Mg^{2+} + 2e^-$$

$$Mg^{2+} + 2OH^- \rightarrow Mg(OH)_2$$

$$Mg(OH)_2 \rightarrow MgO + H_2O$$

$$2Mg^{2+} + SiO_3^{2-} + 2OH^- \rightarrow Mg_2SiO_4 + H_2O$$

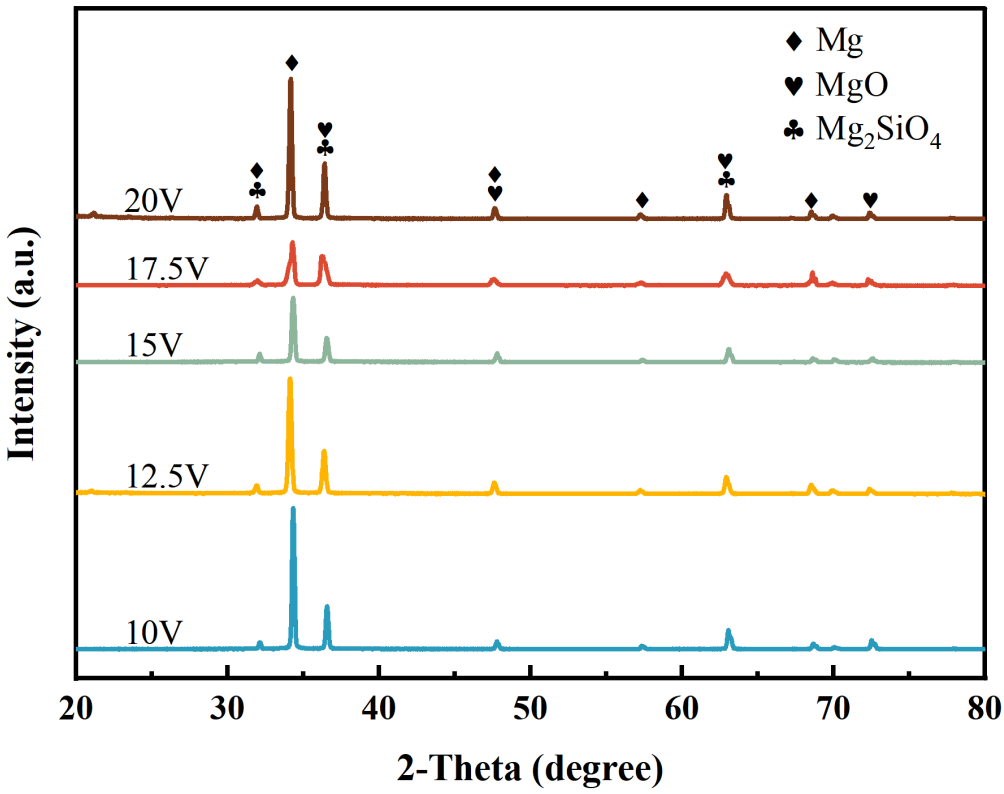

Figure 4. XRD pattern of AZ31B magnesium alloy anodic oxide film.

In the initial stages of anodic oxidation, the oxide film on the AZ31B magnesium alloy is relatively thin and porous. This condition allows for the prominent detection of the AZ31B substrate's diffraction peaks, notably enhancing the Mg peaks observed in XRD analyses. However, with increasing oxidation voltage, there is a notable transition in the film's characteristics: porosity diminishes, density increases, and the film's thickness grows. These changes, while seemingly imposing a physical barrier to X-ray penetration, also reflect significant alterations in the film's crystalline structure and phase composition. Such microscopic changes can profoundly influence the interaction of X-rays with the material, beyond mere physical obstruction. At an oxidation voltage of 17.5 V, this complex interplay results in a marked attenuation of the Mg diffraction peak, as evidenced in Figure 4. This observation is not solely attributable to increased film thickness but is also a manifestation of the enhanced density and altered crystalline structure of the oxide layer, as corroborated by the cross-sectional morphology of the anodically oxidized AZ31B surface [44–46]. These findings suggest that the variations in XRD patterns are indicative of the nuanced effects of anodic oxidation on the material's microstructure, offering insights into the intricate relationship between surface treatment conditions and material properties.

3.4. Electrochemical Performance of Anodized Samples

Electrochemical tests were conducted to further investigate the barrier properties of the oxide film. Figure 5 displays the electrochemical curves of the samples before and after anodizing in a corrosive solution. Compared to the substrate, anodizing shifted the Tafel curves towards higher potential values and lower current densities. The extracted corrosion potential (E_{corr}) and corrosion current density (I_{corr}) from Figure 5a are detailed in Table 1. Under anodizing voltages of 10, 12.5, 15, 17.5, and 20 V, the E_{corr} of AZ31B shifted from −0.25 mV to −0.11 mV, −0.05 mV, 0.06 mV, 0.04 mV, and 0.07 mV, respectively; simultaneously, I_{corr} decreased from 9.4×10^{-4} A/cm^2 to 5.02×10^{-4}, 7.93×10^{-4}, 1.04×10^{-3}, 4.43×10^{-5}, and 8.48×10^{-5} A/cm^2, respectively. The corrosion potential is a thermodynamic measure of a material's susceptibility to corrosion, with a more positive

E_{corr} indicating a lower likelihood of corrosion. The corrosion current density indicates the rate of corrosion under kinetic conditions, with a lower I_{corr} corresponding to a reduced rate of corrosion [47–51].

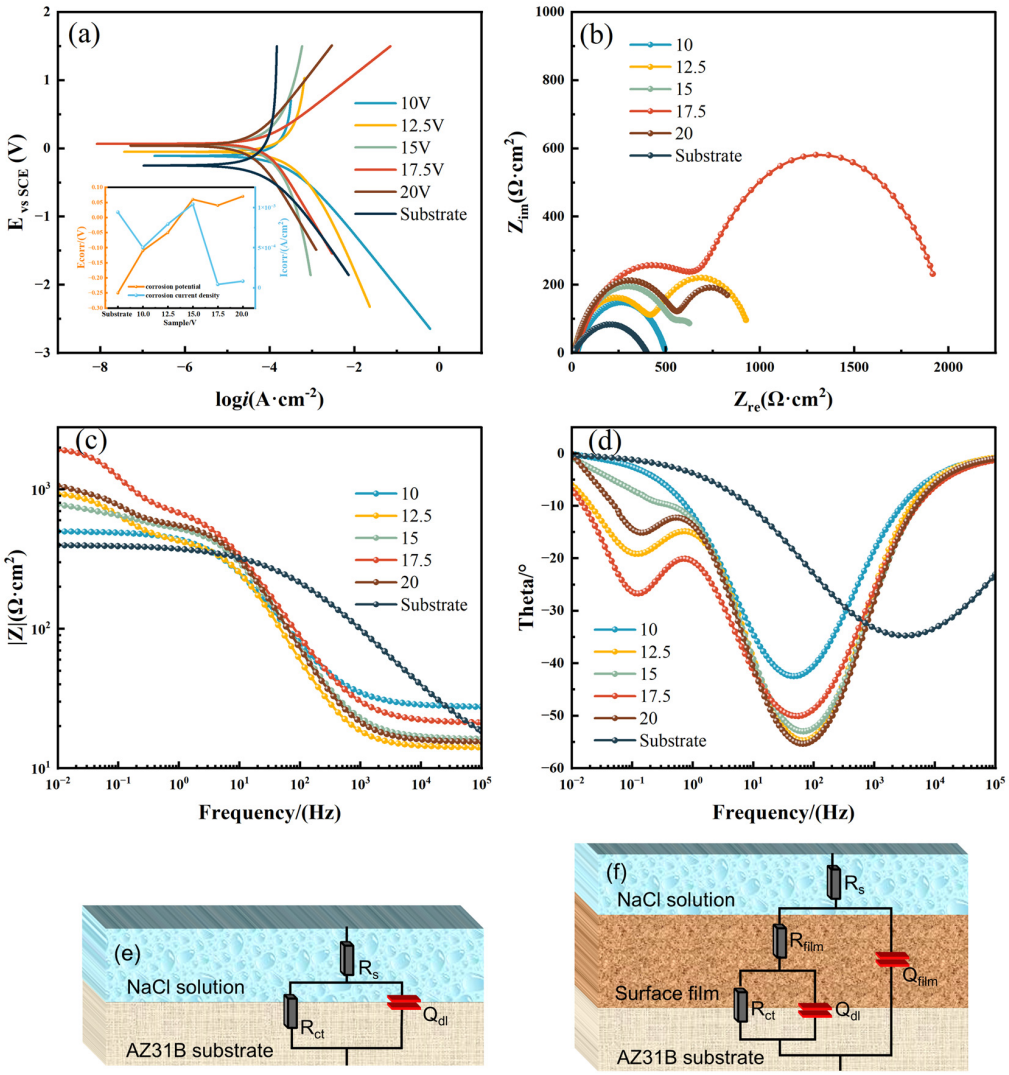

Figure 5. Electrochemical test diagram after substrate and coating treatment: (**a**) Tafel, (**b**) Nyquist plots, (**c**) Bode impedance plots, (**d**) Bode phase plots, (**e**) Equivalent circuit diagram for the analysis of the matrix, and (**f**) Equivalent circuit diagram for the analysis of anodic oxidation.

Table 1. The fitting result of the potentiodynamic polarization curve.

Sample	E_{corr}	I_{corr}	β_α	$\lvert\beta_c\rvert$	R_p
	(Vvs.SCE)	(A/cm^2)	(V/dec)	(V/dec)	($k\Omega/cm^2$)
Substrate	−0.25	9.4×10^{-4}	0.93	63.9	0.42
10 V	−0.11	5.02×10^{-4}	1.11	82.5	0.95
12.5 V	−0.05	7.93×10^{-4}	1.54	94.7	0.83
15 V	0.06	1.04×10^{-3}	9.02	14.8	2.35
17.5 V	0.04	4.43×10^{-5}	1.05	0.81	4.49
20 V	0.07	8.48×10^{-5}	1.04	0.49	1.71

Based on the calculations from the Tafel slope extrapolation method, the corrosion parameters of the anodized AZ31B magnesium alloy films were determined, as shown in Table 1. Polarization resistance (R_p) is another parameter describing the rate of electrode

corrosion, reflecting the resistance to reaction caused by various factors in the electrochemical process. The R_p values under different conditions reached 0.42, 0.95, 0.83, 2.35, 4.49, and 1.71 kΩ/cm^2, respectively. An increase in R_p indicates a decrease in corrosion rate [52,53].

The formula for calculating R_p is as follows:

$$R_p = \frac{\beta_a \beta_c}{2.303 I_{corr}(\beta_a + \beta_c)}$$

where I_{corr} represents the corrosion current density (A·cm^2), and β_a and β_c represent the Tafel slopes for anodic and cathodic reactions, respectively (V/dec).

The polarization curves of the anodized films were almost symmetrically distributed on both sides of the corrosion potential, indicating complete activation of the film at this stage [54,55]. Compared to the substrate, the overall E_{corr} of the anodized films shifted in the positive direction, and R_p increased with voltage, while I_{corr} decreased, indicating enhanced corrosion resistance of the anodized AZ31B magnesium alloy. An increase in corrosion current density accelerated the corrosion rate of the film, whereas a rise in corrosion potential reduced the tendency for corrosion [56,57].

Figure 5b presents the Nyquist plots of the samples before and after anodization. Notably, the anodized samples showed a significant increase in capacitive arc radius, indicating an increase in polarization resistance at the liquid–film–metal interface [58]. Micropores in the oxide film are the primary pathways for corrosive media to penetrate the film, detrimental to substrate protection. A reduction in the number of micropores in the dense film layer significantly hindered the penetration and diffusion of corrosive fluids, thereby reducing the contact area between the corrosive fluid and the substrate and improving the film's corrosion resistance [59]. With increasing voltage, the film density increased, reducing the tendency for corrosion of the anodized film layer, thereby lowering the corrosion rate and effectively inhibiting corrosion in the anodized samples [33].

Figure 5c,d display the Bode plots for each sample. In the high-frequency range, the impedance modulus |Z| tends to a constant value independent of frequency, indicating control by solution resistance. In the mid- and low-frequency regions, linear sections on the curve typically reflect the characteristic response of the passive film capacitance. Figure 5d illustrates two types of corrosion observed during the testing process. In the first process, the simulated body fluid permeates through defects like pores and cracks on the film's surface. In the second one, the substrate surface is also exposed to certain ions that promote corrosion.

Figure 5e,f show the equivalent circuit diagrams of the substrates before and after oxidation treatment [60]. In the diagrams, Rs represents the solution resistance, R_{film} the film resistance, and R_{ct} the charge transfer resistance. Additionally, Q_{film} corresponds to the film capacitance and Q_{dl} to the capacitance at the sample–solution interface. The electrochemical data calculated are detailed in Table 2. The analysis indicates that, after anodizing treatment, the R values exceed those of the untreated samples. The order of R values from lowest to highest is: substrate < 10 < 20 < 12.5 < 15 < 17.5. Tafel analysis and Electrochemical Impedance Spectroscopy (EIS) results confirm that anodizing significantly enhances the corrosion resistance of AZ31B, ultimately forming an oxide film.

Table 2. EIS impedance map fitting results.

Sample	R_s	Q_{film}	n_{film}	R_{film}	Q_{dl}	n_{dl}	R_{ct}	$R = R_f + R_{ct}$
	(Ω/cm^2)	(μS·cm^{-2}·s^{-n})		(Ω/cm^2)	(μS·cm^{-2}·s^{-n})		(Ω/cm^2)	(Ω/cm^2)
Substrate	19.8				88.9	0.516	281	281
10 V	17.4	43.6	0.799	50.7	46.7	0.917	593	643.7
12.5 V	14.1	97	0.812	432	393	0.845	525	957
15 V	15.1	86.4	0.798	685	468	0.951	134	819
17.5 V	21.0	113	0.732	776	179	0.926	1210	1986
20 V	16.1	97.6	0.777	658	746	0.977	318	976

4. Discussion

Corrosion Protection Mechanism

As depicted in Figure 6, from a macroscopic perspective, the primary role of anodizing is to form a uniform protective oxide layer on the magnesium alloy surface. This layer acts as a physical barrier, preventing direct contact of the base metal with corrosive environments (such as air, water, or chemicals) [61]. The anodized coating, being an integral part of the metal, uniformly covers the entire surface, including hard-to-reach areas, crevices, and pits, which are potential corrosion sites on untreated metal.

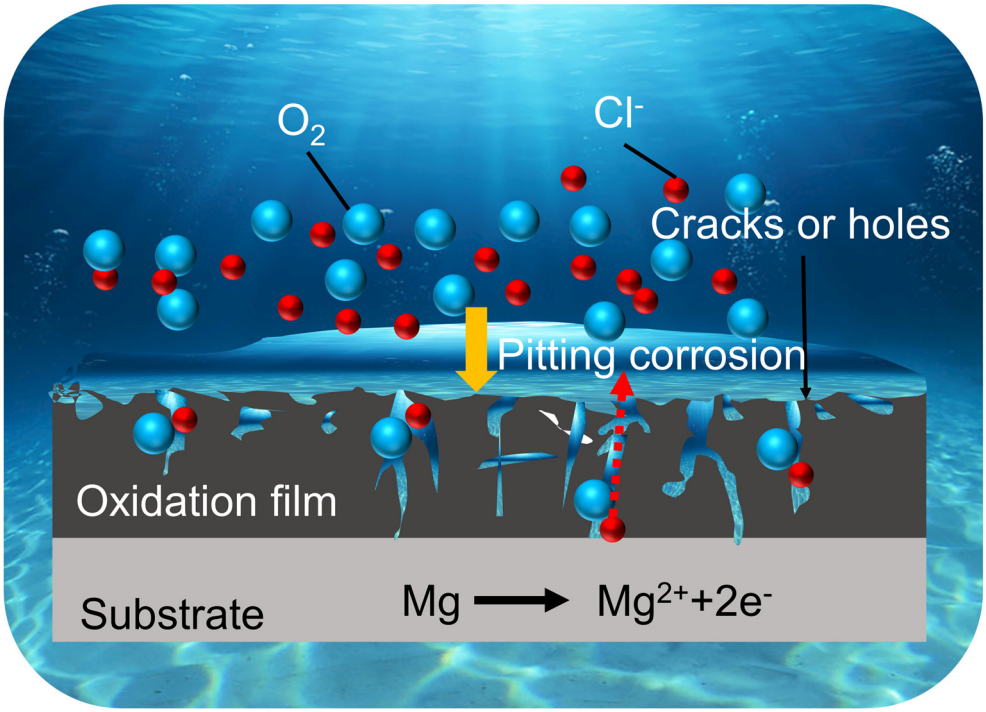

Figure 6. Corrosion mechanism diagram of anodic oxidation coating.

Microscopically, the nature of the oxide layer itself is crucial. Composed of magnesium oxide (MgO), it has a dense crystalline structure, is less reactive than bare magnesium, and is more stable [62]. Anodizing leads to passivation of the magnesium surface, meaning the oxide layer reduces surface reactivity, a key factor in enhancing corrosion resistance. The micro-porous structure within the anodized layer is also significant. The sizes, distributions, and densities of these pores determine the layer's ability to resist corrosive elements. Smaller, denser pores offer better protection. At the molecular level, the anodized layer increases the electrochemical stability of the magnesium alloy. It raises the breakdown potential and lowers the current density, making the underlying metal less susceptible to electrochemical corrosion processes. The anodized layer is more than just a physical covering; it chemically bonds with the underlying magnesium alloy. This atomic-level strong adhesion ensures that the protective layer is firmly attached and less likely to delaminate or crack, which is crucial for long-term corrosion resistance.

5. Conclusions

In conclusion, our comprehensive study on the anodic oxidation of AZ31B magnesium alloy has elucidated the significant impact of varying oxidation voltages on the microstructure, phase composition, and corrosion resistance of the resulting oxide films. Through meticulous experimentation, we identified that anodic oxidation performed at 17.5 V optimally enhances the oxide film's thickness, uniformity, and protective capabilities, evidenced by the formation of predominant MgO and Mg_2SiO_4 phases. This optimal voltage setting not only maximizes the corrosion resistance but also significantly improves the alloy's

electrochemical stability, as demonstrated by the positive shift in corrosion potential and the reduction in corrosion current density.

By establishing a direct link between specific oxidation conditions and the enhanced protective qualities of the oxide film, this research contributes a crucial piece of knowledge to the ongoing efforts to mitigate the corrosion vulnerability of magnesium alloys. The ability to reliably produce a dense, uniform, and corrosion-resistant oxide layer opens new avenues for the application of magnesium alloys across a variety of industries, including automotive, aerospace, and consumer electronics, where weight reduction without compromising durability is a key objective.

Furthermore, our study sets the groundwork for future research in the field, suggesting avenues for exploring the interactions between different anodic oxidation parameters and their collective impacts on the alloy's performance. The methodologies and insights derived from this work offer valuable guidelines for the development of more effective corrosion protection strategies, promoting the wider adoption and long-term sustainability of magnesium alloys in corrosive environments. In essence, our research not only advances the understanding of anodic oxidation as a vital surface treatment for magnesium alloys but also underscores the potential for engineering more resilient materials that align with the principles of lightweight design and environmental sustainability.

Author Contributions: Y.K.: Writing—original draft, Methodology, Investigation, Conceptualization, Formal Analysis. S.Y.: Writing—review and editing, Funding Acquisition, Resources, Conceptualization. Z.L.: Conceptualization, Resources, Data curation, Validation, Visualization. Z.W.: Methodology, Resources, Investigation. A.Y.: Methodology, Investigation. W.M.: Software, Data Curation, Supervision. W.C.: Resources, Supervision, Project administration, Funding acquisition. Y.Q.: Supervision, Project administration. All authors have read and agreed to the published version of the manuscript.

Funding: This research was supported by the Inner Mongolia Autonomous Region science and technology plan project (project No. 2021GG0262), and the National Natural Science Foundation of China (51964035).

Institutional Review Board Statement: Not Applicable.

Informed Consent Statement: Not Applicable.

Data Availability Statement: Data will be made available on request by contacting the corresponding author.

Conflicts of Interest: Yinhui Qu was employed by the company Shenyang Research Institute of Foundry Co., Ltd, The remaining authors declare that the research was conducted in the absence of any commercial or financial relationships that could be construed as a potential conflict of interest.

References

1. Wang, W.; Han, P.; Peng, P.; Zhang, T.; Liu, Q.; Yuan, S.; Huang, L.-Y.; Yu, H.; Qiao, K.; Wang, K. Friction Stir Processing of Magnesium Alloys: A Review. *Acta Metall. Sin. Engl. Lett.* **2019**, *33*, 43–57. [CrossRef]
2. Çelik, I. Structure and surface properties of Al_2O_3–TiO_2 ceramic coated AZ31 magnesium alloy. *Ceram. Int.* **2016**, *42*, 13659–13663. [CrossRef]
3. Bai, J.; Yang, Y.; Wen, C.; Chen, J.; Zhou, G.; Jiang, B.; Peng, X.; Pan, F. Applications of magnesium alloys for aerospace: A review. *J. Magnes. Alloys* **2023**, *11*, 3609–3619. [CrossRef]
4. Zhan, W.; Tian, F.; Ou-Yang, G.; Gui, B.-Y. Effects of Nickel Additive on Micro-Arc Oxidation Coating of AZ63B Magnesium Alloy. *Int. J. Precis. Eng. Manuf.* **2018**, *19*, 1081–1087. [CrossRef]
5. Tan, J.; Ramakrishna, S. Applications of Magnesium and Its Alloys: A Review. *Appl. Sci.* **2021**, *11*, 6861. [CrossRef]
6. Shu, Y.; Peng, F.; Xie, Z.-H.; Yong, Q.; Wu, L.; Xie, J.; Li, M. Well-oriented magnesium hydroxide nanoplatelets coating with high corrosion resistance and osteogenesis on magnesium alloy. *J. Magnes. Alloys*, 2023; *in press*. [CrossRef]
7. Atrens, A.; Song, G.-L.; Cao, F.; Shi, Z.; Bowen, P.K. Advances in Mg corrosion and research suggestions. *J. Magnes. Alloys* **2013**, *1*, 177–200. [CrossRef]
8. Yin, Z.-Z.; Qi, W.; Zeng, R.; Chen, X.-B.; Gu, C.; Guan, S.; Zheng, Y.-F. Advances in coatings on biodegradable magnesium alloys. *J. Magnes. Alloys* **2020**, *8*, 42–65. [CrossRef]
9. Macwan, A.; Jiang, X.; Chen, D. Interfacial Characterization of Dissimilar Joints Between Al/Mg/Al-Trilayered Clad Sheet to High-Strength Low-Alloy Steel. *JOM* **2015**, *67*, 1468–1477. [CrossRef]

10. Karakulak, E. A review: Past, present and future of grain refining of magnesium castings. *J. Magnes. Alloys* **2019**, *7*, 355–369. [CrossRef]
11. Wang, Q.; Jiang, B.; Chen, D.L.; Jin, Z.; Zhao, L.; Yang, Q.; Huang, G.; Pan, F. Strategies for enhancing the room-temperature stretch formability of magnesium alloy sheets: A review. *J. Mater. Sci.* **2021**, *56*, 12965–12998. [CrossRef]
12. Radha, R.; Sreekanth, D. Insight of magnesium alloys and composites for orthopedic implant applications—A review. *J. Magnes. Alloys* **2017**, *5*, 286–312. [CrossRef]
13. Wan, D.; Xue, Y.; Hu, J.; Wang, H.; Liu, W. Corrosion and chemical behavior of Mg97Zn1Y2-1wt.%SiC under different corrosion solutions. *China Foundry* **2021**, *18*, 68–74. [CrossRef]
14. Ramesh, S.; Viswanathan, R.; Ambika, S. Measurement and optimization of surface roughness and tool wear via grey relational analysis, TOPSIS and RSA techniques. *Measurement* **2016**, *78*, 63–72. [CrossRef]
15. Chen, L.; Xu, J.; Choi, H.; Pozuelo, M.; Ma, X.; Bhowmick, S.; Yang, J.-M.; Mathaudhu, S.; Li, X.-C. Processing and properties of magnesium containing a dense uniform dispersion of nanoparticles. *Nature* **2015**, *528*, 539–543. [CrossRef]
16. Shuai, C.; Wang, B.; Yang, Y.; Peng, S.; Gao, C. 3D honeycomb nanostructure-encapsulated magnesium alloys with superior corrosion resistance and mechanical properties. *Compos. Part B Eng.* **2019**, *162*, 611–620. [CrossRef]
17. Luo, Q.; Guo, Y.; Liu, B.; Feng, Y.; Zhang, J.; Li, Q.; Chou, K. Thermodynamics and kinetics of phase transformation in rare earth–magnesium alloys: A critical review. *J. Mater. Sci. Technol.* **2020**, *44*, 171–190. [CrossRef]
18. Zheng, Z. Study on electrochemical corrosion behaviors of AZ31 magnesium alloys in NaCl solution. *J. Shenyang Norm. Univ.* **2004**. Available online: https://consensus.app/papers/study-corrosion-behaviors-az31-magnesium-alloys-nacl-zhiguo/14718c541b0759ac854ce00c1660bff0/ (accessed on 16 February 2024).
19. Li, Z.; Yan, S.; Chen, W.; Zhang, Z.; Kang, Y.; Ma, W. The effect of current density on the anodic oxidation hydrogen barrier film on ZrH1.8 surface. *Corros. Sci.* **2024**, *227*, 111740. [CrossRef]
20. Wang, S.; Zhai, B.; Zhang, B. The effect of the microstructure of porous alumina films on the mechanical properties of glass-fiber-reinforced aluminum laminates. *Compos. Interfaces* **2014**, *21*, 381–393. [CrossRef]
21. Lee, C.-L.; Lin, T.-S.; Kuo, C.; Hsieh, S.; Chen, Y.-C.; Ou, S.; Lin, J.-H.; Ma, C.-H. Anti-fracture performance of micro-arc oxidization films on TiNiSi shape memory alloy after elongation, bending and shape recovery. *Surf. Coat. Technol.* **2019**, *359*, 495–510. [CrossRef]
22. Schwirn, K.; Lee, W.-S.; Hillebrand, R.; Steinhart, M.; Nielsch, K.; Gösele, U. Self-ordered anodic aluminum oxide formed by H_2SO_4 hard anodization. *ACS Nano* **2008**, *2*, 302–310. [CrossRef]
23. Li, W.; Li, W.; Zhu, L.; Liu, H.; Wang, X. Non-sparking anodization process of AZ91D magnesium alloy under low AC voltage. Mater. *Sci. Eng. B-Adv. Funct. Solid-State Mater.* **2013**, *178*, 417–424. [CrossRef]
24. Ko, Y.; Lee, E.S.; Shin, D. Influence of voltage waveform on anodic film of AZ91 Mg alloy via plasma electrolytic oxidation: Microstructural characteristics and electrochemical responses. *J. Alloy. Compd.* **2014**, *586*, S357–S361. [CrossRef]
25. Jang, Y.; Kim, Y.-K.; Park, I.; Lee, S.-J.; Lee, M.-H.; Yoon, J.-M.; Bae, T. Film characteristics of anodic oxidized AZ91D magnesium alloy by applied power. *Surf. Interface Anal.* **2009**, *41*, 524–530. [CrossRef]
26. Yang, K.; Huang, H.; Chen, J.; Cao, B. Discharge Behavior and Dielectric Breakdown of Oxide Films during Single Pulse Anodizing of Aluminum Micro-Electrodes. *Materials* **2019**, *12*, 2286. [CrossRef]
27. Boinet, M.; Verdier, S.; Maximovitch, S.; Dalard, F. Plasma electrolytic oxidation of AM60 magnesium alloy: Monitoring by acoustic emission technique. Electrochemical properties of coatings. *Surf. Coat. Technol.* **2005**, *199*, 141–149. [CrossRef]
28. Frano, A.; Bluschke, M.; Xu, Z.; Frandsen, B.; Lu, Y.; Yi, M.; Marks, R.; Mehta, A.; Borzenets, V.; Meyers, D.; et al. Control of dopant crystallinity in electrochemically treated cuprate thin films. *Phys. Rev. Mater.* **2019**, *3*, 063803. [CrossRef]
29. Kowarik, S.; Gerlach, A.; Sellner, S.; Schreiber, F.; Cavalcanti, L.; Konovalov, O. Real-time observation of structural and orientational transitions during growth of organic thin films. *Phys. Rev. Lett.* **2006**, *96*, 125504. [CrossRef] [PubMed]
30. Duan, H.; Yan, C.; Wang, F. Effect of electrolyte additives on performance of plasma electrolytic oxidation films formed on magnesium alloy AZ91D. *Electrochim. Acta* **2007**, *52*, 3785–3793. [CrossRef]
31. Chernyakova, K.; Vrublevsky, I.; Jagminas, A.; Klimas, V. Effect of anodic oxygen evolution on cell morphology of sulfuric acid anodic alumina films. *J. Solid State Electrochem.* **2021**, *25*, 1453–1460. [CrossRef]
32. Vanhumbeeck, J.; Proost, J. On the Relation Between Growth Instabilities and Internal Stress Evolution during Galvanostatic Ti Thin Film Anodization. *J. Electrochem. Soc.* **2008**, *155*, C506–C514. [CrossRef]
33. Ono, S.; Moronuki, S.; Mori, Y.; Koshi, A.; Liao, J.; Asoh, H. Effect of Electrolyte Concentration on the Structure and Corrosion Resistance of Anodic Films Formed on Magnesium through Plasma Electrolytic Oxidation. *Electrochimica Acta* **2017**, *240*, 415–423. [CrossRef]
34. Zhang, J.; Yang, D.; Ou, X. Microstructures and properties of aluminum film and its effect on corrosion resistance of AZ31B substrate. *Trans. Nonferrous Met. Soc. China* **2008**, *18*, s312–s317. [CrossRef]
35. Lee, Y.K.; Lee, K.-S.; Jung, T. Study on microarc oxidation of AZ31B magnesium alloy in alkaline metal silicate solution. *Electrochem. Commun.* **2008**, *10*, 1716–1719. [CrossRef]
36. Asoh, H.; Matsuoka, S.; Sayama, H.; Ono, S. Anodizing under sparking of AZ31B magnesium alloy in Na_3PO_4 electrolyte. *J. Jpn. Inst. Light Met.* **2010**, *60*, 608–614. [CrossRef]
37. Diamanti, M.V.; Pedeferri, M.P. Effect of anodic oxidation parameters on the titanium oxides formation. *Corros. Sci.* **2007**, *49*, 939–948. [CrossRef]

38. Bai, A.; Chen, Z.-J. Effect of electrolyte additives on anti-corrosion ability of micro-arc oxide coatings formed on magnesium alloy AZ91D. *Surf. Coat. Technol.* **2009**, *203*, 1956–1963. [CrossRef]
39. Hahn, R.; Brunner, J.G.; Kunze, J.; Schmuki, P.; Virtanen, S. A novel approach for the formation of $Mg(OH)_2$/MgO nanowhiskers on magnesium: Rapid anodization in chloride containing solutions. *Electrochem. Commun.* **2008**, *10*, 288–292. [CrossRef]
40. Thomas, S.; Medhekar, N.; Frankel, G.; Birbilis, N. Corrosion mechanism and hydrogen evolution on Mg. *Curr. Opin. Solid State Mater. Sci.* **2015**, *19*, 85–94. [CrossRef]
41. He, Y. An application study of special MgO to oriented silicon steel. *Trans. Mater. Heat Treat.* **2011**. Available online: https://consensus.app/papers/application-study-oriented-silicon-steel-yedong/54bc4e3d68805dce8465037bc8979ae9/ (accessed on 18 January 2024).
42. Martin, G.B.; Spera, F.; Ghiorso, M.; Nevins, D. Structure, thermodynamic, and transport properties of molten Mg_2SiO_4: Molecular dynamics simulations and model EOS. *Am. Miner.* **2009**, *94*, 693–703. [CrossRef]
43. Niu, H.; Oganov, A.; Chen, X.-Q.; Li, D. Prediction of novel stable compounds in the Mg-Si-O system under exoplanet pressures. *Sci. Rep.* **2015**, *5*, 18347. [CrossRef]
44. Zuraidawani, C.D.; Norhadira, F.W.; Derman, M. Synthesis and Characterisation of Anodized Powder Metallurgy Mg-Ca Alloy. *Solid State Phenom.* **2018**, *280*, 221–225. [CrossRef]
45. Si, H.; Sun, Z.-H.; Kang, X.; Zi, W.; Zhang, H.-L. Voltage-dependent morphology, wettability and photocurrent response of anodic porous titanium dioxide films. *Microporous Mesoporous Mater.* **2009**, *119*, 75–81. [CrossRef]
46. Kim, S.-J.; Okido, M. The Electrochemical Properties and Mechanism of Formation of Anodic Oxide Films on Mg-Al Alloys. *Bull. Korean Chem. Soc.* **2003**, *24*, 975–980. [CrossRef]
47. CherylLyne, C. An artificial neural network model for the corrosion current density of steel in mortar mixed with seawater. *Int. J. GEOMATE* **2019**, *16*, 79–84. [CrossRef]
48. Andrade, C. Electrochemical methods for on-site corrosion detection. *Struct. Concr.* **2020**, *21*, 1385–1395. [CrossRef]
49. Starosta, R. Influence of Seawater Salinity on Corrosion of Austenitic Steel. *J. KONES* **2019**, *26*, 219–225. [CrossRef]
50. Asri, N.F.; Husaini, T.; Sulong, A.B.; Majlan, E. Effects of the Synthesis Coating Parameters for Metal Bipolar Plates. *Sains Malays.* **2020**, *49*, 3179–3188. [CrossRef]
51. Nyby, C.; Guo, X.; Saal, J.; Chien, S.-C.; Gerard, A.Y.; Ke, H.; Li, T.; Lu, P.; Oberdorfer, C.; Sahu, S.; et al. Electrochemical metrics for corrosion resistant alloys. *Sci. Data* **2021**, *8*, 58. [CrossRef] [PubMed]
52. Attarzadeh, N.; Ramana, C.V. Plasma Electrolytic Oxidation Ceramic Coatings on Zirconium (Zr) and Zr-Alloys: Part-II: Properties and Applications. *Coatings* **2021**, *11*, 620. [CrossRef]
53. Polder, R.; Cigna, R. Test methods for on-site corrosion rate measurement of steel reinforcement in concrete by means of the polarization resistance method. *Mater. Struct.* **2004**, *37*, 623–643. [CrossRef]
54. Frankel, G. Fundamentals of Corrosion Kinetics. *Act. Prot. Coat.* **2016**, *233*, 17–32. [CrossRef]
55. Li, Y.J.; Wang, Y.; An, B.; Xu, H.; Liu, Y.; Zhang, L.C.; Ma, H.; Wang, W.M. A Practical Anodic and Cathodic Curve Intersection Model to Understand Multiple Corrosion Potentials of Fe-Based Glassy Alloys in OH- Contained Solutions. *PLoS ONE* **2016**, *11*, e0146421. [CrossRef]
56. Parthiban, G.; Malarkodi, D.; Palaniswamy, N.; Venkatachari, G. Corrosion protection by acrylamide treatment for magnesium alloy metal matrix composite (MMC) reinforced with titanium boride. *Surf. Eng.* **2010**, *26*, 378–384. [CrossRef]
57. Supriyono, R.O.; Wulaningfitri, L.P.M.; Pradana, J.C.; Feliana, I. Influence of anodizing concentration and electric potential on surface morphology and corrosion behavior of anodized magnesium in seawater activated battery. *IOP Conf. Ser. Earth Environ. Sci.* **2018**, *105*, 012054. [CrossRef]
58. Zhang, G.; Wu, L.; Tang, A.; Ma, Y.; Song, G.-L.; Zheng, D.; Jiang, B.; Atrens, A.; Pan, F. Active corrosion protection by a smart coating based on a MgAl-layered double hydroxide on a cerium-modified plasma electrolytic oxidation coating on Mg alloy AZ31. *Corros. Sci.* **2018**, *139*, 370–382. [CrossRef]
59. Stern, M.; Geary, A.L. Electrochemical Polarization: I. A Theoretical Analysis of the Shape of Polarization Curves. *J. Electrochem. Soc.* **1957**, *104*, 56. [CrossRef]
60. Karimi, M.; Shayegh Boroujeny, B.; Adelkhani, H. The effect of zirconium hydride on the corrosion and mechanical behavior of zirconium base metal: Experimental and simulation studies. *Appl. Surf. Sci. Adv.* **2021**, *6*, 100166. [CrossRef]
61. Rahman, Z.U.; Deen, K.M.; Haider, W. Controlling corrosion kinetics of magnesium alloys by electrochemical anodization and investigation of film mechanical properties. *Appl. Surf. Sci.* **2019**, *484*, 906–916. [CrossRef]
62. Zaffora, A.; Di Franco, F.; Virtù, D.; Pavia, F.C.; Ghersi, G.; Virtanen, S.; Santamaria, M. Tuning of the Mg Alloy AZ31 Anodizing Process for Biodegradable Implants. *ACS Appl. Mater. Interfaces* **2021**, *13*, 12866–12876. [CrossRef]